Singular charge fluctuations at a magnetic quantum critical point

L. Prochaska[1,*], X. Li[2,#,*], D. C. MacFarland[1,3,§,*], A. M. Andrews[3], M. Bonta[4], E. F. Bianco[5], S. Yazdi[6,$], W. Schrenk[7], H. Detz[7,+], A. Limbeck[4], Q. Si[8], E. Ringe[6,×], G. Strasser[3,7], J. Kono[2,6,8], and S. Paschen[1,8,‡]

[1]*Institute of Solid State Physics, TU Wien, Wiedner Hauptstr. 8-10, 1040 Vienna, Austria*

[2]*Department of Electrical and Computer Engineering, 6100 Main Street, Rice University, Houston, Texas 77005, USA*

[3]*Institute of Solid State Electronics, TU Wien, Nanocenter Campus Gußhaus, Gußhausstr. 25-25a, Gebäude CH, 1040 Vienna, Austria*

[4]*Institute of Chemical Technologies and Analytics, TU Wien, Getreidemarkt 9, 1060 Vienna, Austria*

[5]*Department of Chemistry, 6100 Main Street, Rice University, Houston, Texas 77005, USA*

[6]*Department of Materials Science and Nanoengineering, 6100 Main Street, Rice University, Houston, Texas 77005, USA*

[7]*Center for Micro- and Nanostructures, Nanocenter Campus Gußhaus, Gußhausstr. 25-25a, Gebäude CH, 1040 Vienna, Austria*

[8]*Department of Physics and Astronomy, Center for Quantum Materials, 6100 Main Street, Rice University, Houston, Texas 77005, USA*

November 15, 2019

Strange metal behavior is ubiquitous in correlated materials ranging from cuprate superconductors to bilayer graphene. It may arise from physics beyond the quantum fluctuations of a Landau order parameter. In quantum critical heavy fermion antiferromagnets, such physics may be realized as critical Kondo entanglement of spin and charge and probed by optical conductivity. We present terahertz time-domain transmission spectroscopy on molecular beam epitaxy-grown thin films of $YbRh_2Si_2$, a model strange metal compound. We observe frequency over temperature scaling of the optical conductivity as a hallmark of beyond-Landau quantum criticality. Our discovery suggests that critical charge fluctuations play a central role in the strange metal behavior, thereby elucidating one of the long-standing mysteries of correlated quantum matter.

*These authors contributed equally to this work.

#Present address: Department of Physics, California Institute of Technology, Pasadena, CA 91125, USA; Institute for Quantum Information and Matter, California Institute of Technology, Pasadena, CA 91125, USA

§Present address: SUNY - University at Buffalo, Jacobs School of Medicine and Biomedical Sciences, 955 Main Street, Buffalo, NY 14203, USA

$Present address: Renewable and Sustainable Energy Institute, University of Colorado Boulder, Boulder, Colorado 80309, USA

×Present address: Department of Earth Sciences, University of Cambridge, Downing Street, Cambridge, CB2 3EQ, UK; Department of Materials Science and Metallurgy, University of Cambridge, 27 Charles Babbage Road, Cambridge, CB3 0FS, UK

+Present second address: Central European Institute of Technology, Brno University of Technology, Purkyňova 123, Brno, 612 00, CZ

‡To whom correspondence should be addressed; E-mail: paschen@ifp.tuwien.ac.at.

Quantum critical behavior as prescribed by the Landau framework of order parameter fluctuations (*1, 2*) has been clearly identified in insulating quantum magnets such as $LiHoF_4$ (*3*) and $TlCuCl_3$ (*4*). In strongly correlated metals, however, this framework often fails. In the strange metal (*5*) regime of various correlated systems (*6*), electronic localization-delocalization transitions have been reported (*7–14*) and it is an outstanding question whether they are a key ingredient of beyond-Landau quantum criticality. To make progress, it is essential to study the dynamics of charge carriers in a suitable setting.

We chose the heavy fermion metal $YbRh_2Si_2$ (*15*) for our investigation because it has a well-defined quantum critical point (*15, 16*) and shows evidence for an electron localization-delocalization transition (*7, 8*) in its strange metal regime. An ideal tool to study such properties are optical conductivity measurements in the relevant frequency window, which is typically the terahertz (THz) range and below for heavy fermion systems. However, such measurements are challenging on bulk samples because the Kramers-Kronig transformation to extract the real and imaginary parts of the optical conductivity from reflectivity measurements introduces substantial uncertainty at low frequencies (*17*). Thus, we resorted to a different approach: We performed THz time-domain transmission spectroscopy experiments on thin films of $YbRh_2Si_2$ grown by molecular beam epitaxy (MBE). Our measurements reveal ω/T scaling of the optical conductivity, thereby elucidating the mechanism for strange metal phenomena.

To grow epitaxial thin films of $YbRh_2Si_2$ on (THz transparent) Ge substrates (Fig. 1A), we used a specially equipped MBE system (*18*). The epitaxial growth of phase-pure $YbRh_2Si_2$ is confirmed by X-ray diffraction (Fig. 1B) (*18*), and the high quality of the film and the film-substrate interface are revealed by high-resolution transmission electron microscopy (Fig. 1, C and D) (*18*). The temperature dependence of the (quasi) dc electrical resistivity $\rho(T)$ of these films (*18*) is similar to that of bulk single crystals (*15, 19*) (Fig. 2). Most notably, it displays strange metal behavior, $\rho = \rho_0 + A'T^{\alpha}$ (Fig. 2B), with an exponent α that strongly deviates

from the Fermi liquid value $\alpha = 2$, and tends to $\alpha = 1$ in the low-temperature limit (Fig. S1).

The frequency dependence of the real part of the complex optical conductivity, $\mathrm{Re}(\sigma)$, measured at temperatures between 1.4 and 250 K and frequencies between 0.25 and 2.6 THz, is shown in Fig. 3A (see Fig. S2 for the imaginary part, $\mathrm{Im}(\sigma)$). The dc electrical conductivity $\sigma = 1/\rho$ values, plotted as symbols at $\omega = 0$, are compatible with the extrapolation of the finite frequency results to zero frequency. Both $\mathrm{Re}(\sigma)$ and $\mathrm{Im}(\sigma)$ are flat and featureless at temperatures above about 80 K (indicating strong incoherent scattering of charges), but develop sizeable temperature and frequency dependence at lower temperatures, with spectral weight of $\mathrm{Re}(\sigma)$ being transferred to low frequencies. The increasingly sharp and pronounced resonance of $\mathrm{Re}(\sigma)$, with non-Lorentzian shape (i.e., non-Drude behavior, see Fig. S3), may, in clean samples, be associated with non-Fermi liquid behavior. These results confirm deviations from simple Drude behavior seen earlier in optical reflectivity measurements in the far-infrared range on bulk $YbRh_2Si_2$ single crystals (*20*).

To explore dynamical scaling, we analyze the frequency-dependent intrinsic optical conductivity $\sigma_{\mathrm{in}}(\omega)$ by subtracting a residual resistivity due to impurity scattering; this subtraction is motivated by analogy to the Matthiessen's law used for the dc resistivity (*18*). We plot $\mathrm{Re}[\sigma_{\mathrm{in}}(\omega)] \cdot T^{\alpha}$ as a function of $\hbar\omega/(k_{\mathrm{B}}T)$, where $\hbar$ is the Planck constant divided by 2π and k_{B} the Boltzmann constant, for temperatures ($T \leq 15$ K) well below the material's Kondo temperature $T_{\mathrm{K}} = 24$ K (*15*) (Fig. 3B) and frequencies below 2 THz. Indeed, for $\alpha \approx 1$, all curves collapse, demonstrating ω/T scaling of $\mathrm{Re}[\sigma_{\mathrm{in}}(\omega)]$.

How can the optical conductivity, which probes charge fluctuations, show critical ω/T scaling at an antiferromagnetic quantum critical point where, a priori, only spin fluctuations are expected – and indeed observed (*21–23*) – to be critical? A natural way for this to happen is to have a critical form of the Kondo entanglement between the local moments and the conduction electrons (*24–26*), as illustrated in Fig. 4. Across the quantum critical point, the conduction

electrons go from being (asymptotically) decoupled from the local moments (bottom left box) to being entangled with them (bottom right box). Correspondingly, the elementary excitations change from separate charge (single conduction electrons/holes) and spin excitations (top left box) to the heavy quasiparticles (top right box) that are hybrids of the slow composite fermions (large tadpole) and the bare conduction electrons (small tadpole). In other words, the single electron excitations capture the continuous onset of the Kondo entanglement at the quantum critical point and are part of the critical degrees of freedom. Thus, optical conductivity, which probes the charge current of the elementary excitations, manifests the singular fluctuations of the QCP. In fact, within the Landau description of a metallic antiferromagnetic quantum critical point (*1, 2*), the slow long-wavelength fluctuations of the order parameter alone describe a Gaussian fixed point, where ω/T scaling is violated. The incorporation of the single electron excitations in the quantum critical spectrum not only makes charge fluctuations part of the quantum criticality, but also turns the fixed point into an interacting one (*24*), thereby leading to ω/T scaling.

Dynamical scaling of the optical conductivity in the region of T-linear resistivity has also been analyzed in an optimally doped Bi-2212 cuprate (*27*). There, different scaling functions are needed in different ω/T ranges, leaving open the question of how the fluctuations of the charge carriers connect with the robust linear-in-temperature resistivity of the cuprate superconductors. By contrast, in the present study of $YbRh_2Si_2$, a single ω/T scaling form is uncovered in its strange metal regime. It is important to explore the dynamical scaling of the optical conductivity in other materials classes with strange metal behavior; one can then assess whether the charge carrier dynamics emerging from a localization-delocalization quantum critical point, as proposed here, is a universal mechanism of strange metal behavior. This scaling form also provides an intriguing link to the quantum scaling of metal-insulator transitions, both in Mott-Hubbard (*28–30*) and in disordered systems (*31*).

Our results demonstrate that charge carriers are a central ingredient of the singular physics at the border of antiferromagnetic order, providing direct evidence for the beyond-Landau nature of metallic quantum criticality. Our findings also delineate the role of electronic localization transitions in strange metal phenomena, which are relevant to a variety of strongly correlated materials (*32*) and beyond (*33*).

REFERENCES AND NOTES

1. J. A. Hertz, *Phys. Rev. B* **14**, 1165 (1976).
2. A. J. Millis, *Phys. Rev. B* **48**, 7183 (1993).
3. D. Bitko, T. F. Rosenbaum, G. Aeppli, *Phys. Rev. Lett.* **77**, 940 (1996).
4. P. Merchant, *et al.*, *Nat. Phys.* **10**, 373 (2014).
5. P. Giraldo-Gallo, *et al.*, *Science* **361**, 479 (2018).
6. J. A. N. Bruin, H. Sakai, R. S. Perry, A. P. Mackenzie, *Science* **339**, 804 (2013).
7. S. Paschen, *et al.*, *Nature* **432**, 881 (2004).
8. S. Friedemann, *et al.*, *Proc. Natl. Acad. Sci. U.S.A.* **107**, 14547 (2010).
9. J. Custers, *et al.*, *Nat. Mater.* **11**, 189 (2012).
10. Y. Luo, *et al.*, *Nat. Mater.* **13**, 777 (2014).
11. F. F. Balakirev, *et al.*, *Nature* **424**, 912 (2003).
12. H. Oike, K. Miyagawa, H. Taniguchi, K. Kanoda, *Phys. Rev. Lett.* **114**, 067002 (2015).
13. S. Badoux, *et al.*, *Nature* **531**, 210 (2016).

14. Y. Cao, *et al.*, *Nature* **556**, 43 (2018).

15. O. Trovarelli, *et al.*, *Phys. Rev. Lett.* **85**, 626 (2000).

16. P. Gegenwart, *et al.*, *Phys. Rev. Lett.* **89**, 056402 (2002).

17. J. Orenstein, *et al.*, *Phys. Rev. B* **42**, 6342 (1990).

18. Materials and methods are available as supplementary materials.

19. T. Westerkamp, Quantenphasenübergänge in den Schwere-Fermionen-Systemen $Yb(Rh_{1-x}M_x)_2Si_2$ und $CePd_{1-x}Rh_x$, Ph.D. thesis, TU Dresden, Germany (2009).

20. S. Kimura, *et al.*, *Phys. Rev. B* **74**, 132408 (2006).

21. M. Aronson, *et al.*, *Phys. Rev. Lett.* **75**, 725 (1995).

22. A. Schröder, *et al.*, *Nature* **407**, 351 (2000).

23. C. Stock, *et al.*, *Phys. Rev. Lett.* **109**, 127201 (2012).

24. Q. Si, S. Rabello, K. Ingersent, J. Smith, *Nature* **413**, 804 (2001).

25. P. Coleman, C. Pépin, Q. Si, R. Ramazashvili, *J. Phys.: Condens. Matter* **13**, R723 (2001).

26. T. Senthil, M. Vojta, S. Sachdev, *Phys. Rev. B* **69**, 035111 (2004).

27. D. van der Marel, *et al.*, *Nature* **425**, 271 (2003).

28. T. Senthil, *Phys. Rev. B* **78**, 035103 (2008).

29. H. Terletska, J. Vučičević, D. Tanasković, V. Dobrosavljević, *Phys. Rev. Lett.* **107**, 026401 (2011).

30. T. Furukawa, K. Miyagawa, H. Taniguchi, R. Kato, K. Kanoda, *Nat. Phys.* **11**, 221 (2015).

31. H.-L. Lee, J. P. Carini, D. V. Baxter, W. Henderson, G. Grüner, *Science* **287**, 633 (2000).

32. B. Keimer, J. E. Moore, *Nat. Phys.* **13**, 1045 (2017).

33. P. T. Brown, *et al.*, *Science* **363**, 379 (2019).

34. Data sets of all figures of this work are available on Zenodo, doi:10.5281/zenodo.3541572.

35. D. Rossi, R. Marazza, R. Ferro, *J. Less-Common Met.* **66**, P17 (1979).

36. L. Gupta, *Theoretical and Experimental Aspects of Valence Fluctuations and Heavy Fermions* (Springer US, 1987).

37. G. Knebel, *et al.*, *J. Phys. Soc. Jpn.* **75**, 114709 (2006).

38. R. Hu, J. Hudis, C. Stock, C. Broholm, C. Petrovic, *J. Cryst. Growth* **304**, 114 (2007).

39. C. Krellner, S. Taube, T. Westerkamp, Z. Hossain, C. Geibel, *Philos. Mag.* **92**, 2508 (2012).

40. J.-P. Reid, *et al.*, *Phys. Rev. B* **89**, 045130 (2014).

41. F. Durand, J. C. Duby, *J. Phase Equilibria* **20**, 61 (1999).

42. L. E. Vorobyev, *Handbook Series on Semiconductor Parameters* (World Scientific, 1996), pp. 33–57.

43. J. H. van der Merwe, *J. Appl. Phys.* **34**, 123 (1963).

44. W. D. Callister, *Fundamentals of Materials Science and Engineering: An Interactive e. Text, 5th Edition* (Wiley, 2000).

45. S. Wirth, *et al.*, *J. Phys.: Condens. Matter* **24**, 294203 (2012).

46. K. Momma, F. Izumi, *J. Appl. Crystallogr.* **44**, 1272 (2011).

47. R. N. Gurzhi, *Sov. Phys. JETP* **35**, 673 (1959).

48. C. Berthod, *et al.*, *Phys. Rev. B* **87**, 115109 (2013).

49. L. Degiorgi, *Rev. Mod. Phys.* **71**, 687 (1999).

50. M. Scheffler, M. Dressel, M. Jourdan, H. Adrian, *Nature* **438**, 1135 (2005).

51. G. Bossé, *et al.*, *Phys. Rev. B* **85**, 155105 (2012).

52. M. Scheffler, *et al.*, *J. Phys. Soc. Jpn.* **82**, 043712 (2013).

53. G. Bossé, *et al.*, *Phys. Rev. B* **93**, 085104 (2016).

ACKNOWLEDGMENTS

We thank P. Gegenwart, Y.-B. Kim, H. von Löhneysen, S. Nakatsuji, H.-C. Nägerl, and A. Prokofiev for useful discussions.

Funding: Financial support for this work was provided by the European Research Council (ERC Advanced Grant 227378), the U.S. Army Research Office (ARO W911NF-14-1-0496), the Austrian Science Fund (FWF W1243, P29279-N27, and P29296-N27), and the European Union's Horizon 2020 research and innovation programme (grant agreement No 824109 – EMP). X.L. and J.K. acknowledge financial support from the National Science Foundation (NSF MRSEC DMR-1720595) and the ARO (W911NF-17-1-0259). Q.S. acknowledges financial support from the NSF (DMR-1920740), the Robert A. Welch Foundation (C-1411), and the ARO (W911NF-14-1-0525), and hospitality of the University of California at Berkeley, the Aspen Center for Physics (NSF grant PHY-1607611), and the Los Alamos National Laboratory (via a Ulam Scholarship from the Center for Nonlinear Studies). This work has also been supported by an InterDisciplinary Excellence Award (IDEA) from Rice University (Q.S., E.R., J.K., S.P.).

Authors contributions: S.P. designed and led the research. L.P., D.C.M., A.M.A., W.S., H.D., and G.S. performed the MBE growth, M.B. and A.L. the analytical characterization, E.B., S.Y., and E.R. the TEM investigation, X.L. and J.K. the THz spectroscopy. Q.S. contributed to the understanding of the results. L.P., X.L., D.C.M., Q.S., and S.P. wrote the manuscript, with contributions from all other authors.

Competing interests: The authors have no competing interests.

Data and materials availability: All data presented in this paper are deposited in Zenodo (*34*).

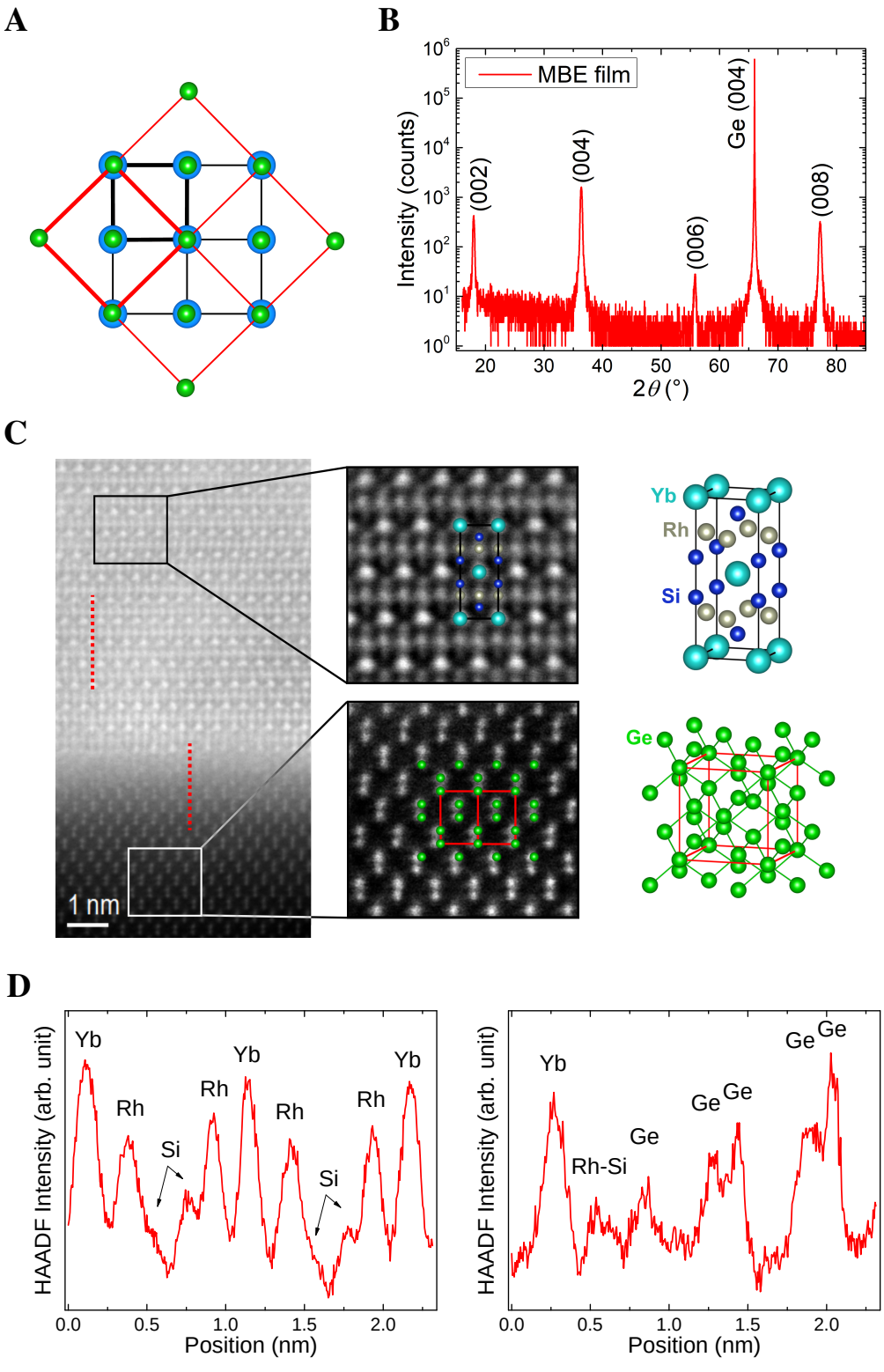
A
B
MBE film
Intensity (counts)
2θ (°)
(002)
(004)
(006)
Ge (004)
(008)
C
1 nm
Yb
Rh
Si
Ge
D
HAADF Intensity (arb. unit)
Position (nm)
Yb
Rh
Si
Rh-Si
Ge

Figure 1: **$YbRh_2Si_2$ thin films grown by molecular beam epitaxy.** (**A**) Visualization of the lattice matching between $YbRh_2Si_2$ (blue circles, black lines) and Ge (green circles, red lines), with the crystallographic c directions pointing out of the plane. For the Yb atoms to associate with the Ge atoms, the respective unit cells (thick lines, see panel **C** right) are rotated by 45° with respect to each other around the c direction. (**B**) High-resolution X-ray diffraction pattern, with all peaks identified as due to the film or Ge substrate, confirming that the film is phase pure $YbRh_2Si_2$. (**C**) Atomic resolution high-angle annular dark field scanning transmission electron microscopy (HAADF-STEM) image of the interface between film (top left) and substrate (bottom left), representative enlarged views with simulated overlays (center), and the corresponding unit cells (right). (**D**) Intensity profiles along the red dashed lines in (**C** left), within the film (upper line, left panel) and across the interface (lower line, right panel).

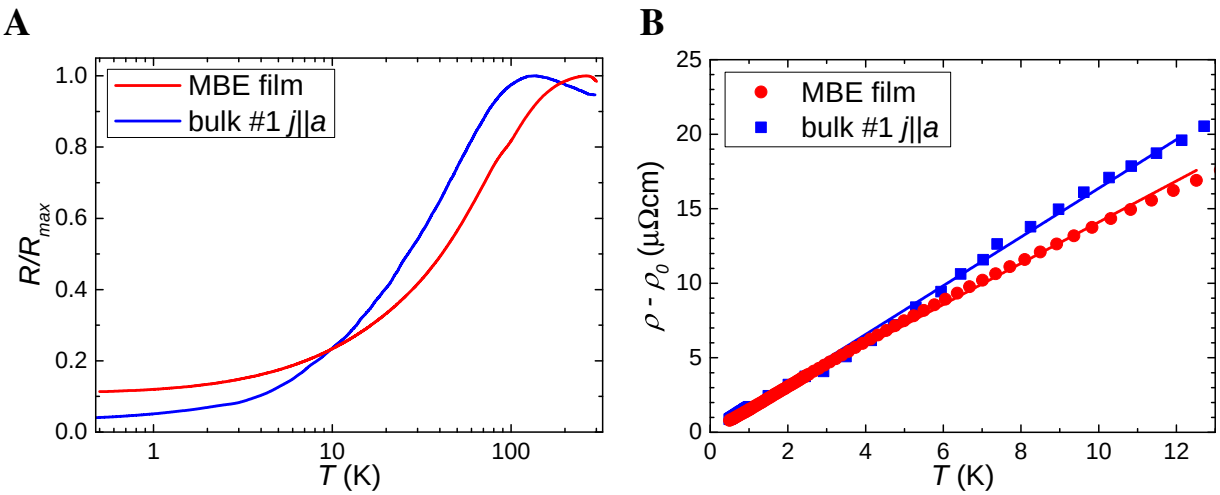

Figure 2: **Electrical resistivity of MBE-grown $YbRh_2Si_2$.** (**A**) Normalized resistance of an MBE-grown $YbRh_2Si_2$ film, and a bulk single crystal with current j within the tetragonal aa plane (*15*) for comparison. The film was measured using the van der Pauw technique. (**B**) Corresponding low-temperature resistivities, with the residual resistivities ($\rho_0 = 11.6\,\mu\Omega$cm and $2.45\,\mu\Omega$cm for the MBE and bulk (*15*) samples, respectively, determined by linear-in-T fits to the data below 1 K) subtracted, displaying non-Fermi liquid behavior (lines represent $\rho - \rho_0 = A'T^{\alpha}$ fits with constant α to the data below 12 K).

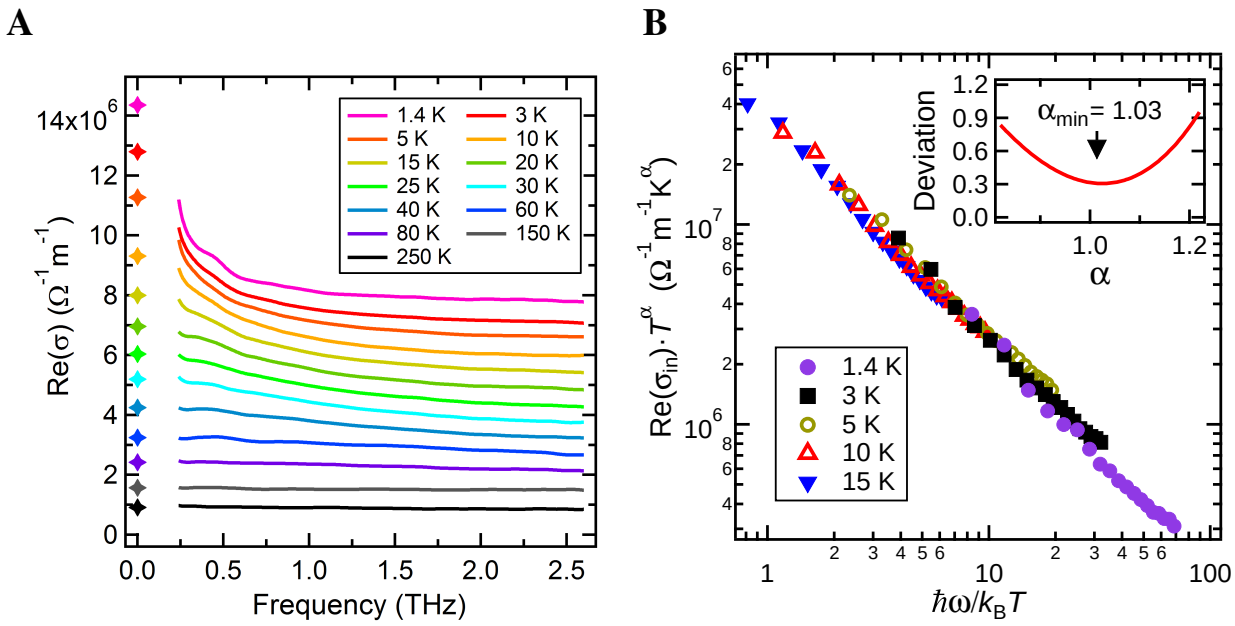

Figure 3: **THz time-domain transmission spectroscopy of MBE-grown $YbRh_2Si_2$.** (**A**) Real part of optical conductivity $\mathrm{Re}(\sigma)$ vs frequency at different temperatures (bottom to top: 250, 150, 80, 60, 40, 30, 25, 20, 15, 10, 5, 3, 1.4 K), with corresponding dc values marked as zero-frequency points. Curves below 250 K (and the respective dc values) are successively offset by $6 \times 10^5\,\Omega^{-1}\mathrm{m}^{-1}$ for clarity. (**B**) ω/T scaling, with a critical exponent of $\alpha \approx 1$, revealed by $\mathrm{Re}[\sigma_{\mathrm{in}}(\omega)] \cdot T^{\alpha}$ isotherms plotted vs $\hbar\omega/(k_{\mathrm{B}}T)$ collapsing onto a single curve for temperatures $T \leq 15\,\mathrm{K}$ and frequencies below 2 THz. Inset: Normalized deviation between the different isotherms as a function of α, revealing best scaling for $\alpha = 1.03$.

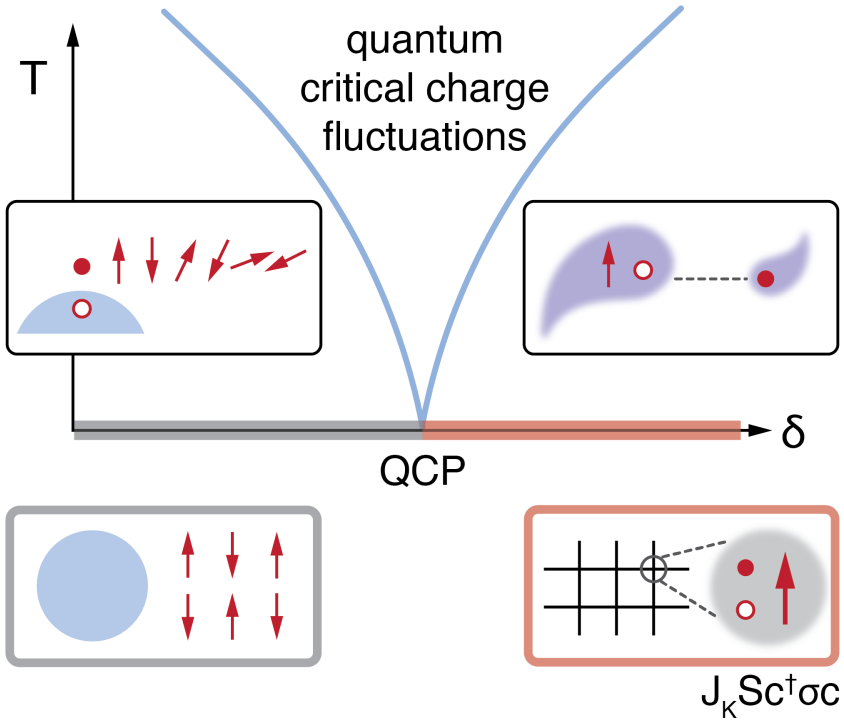

Figure 4: **Illustration of quantum critical charge fluctuations emerging from Kondo disentanglement.** Tuning a heavy fermion metal with a non-thermal parameter δ, which microscopically corresponds to the ratio of Kondo to RKKY coupling, from an antiferromagnetic ground state with local moment order (bottom left box; circle and arrows represent Fermi sphere and local moments, respectively) to a Kondo entangled paramagnet (bottom right box; the antiferromagnetic Kondo exchange J_K favors the formation of a Kondo singlet between the local moment S, represented as arrow, and the spin of the conduction electrons $c^\dagger \sigma c$, i.e., the particle-hole excitation of the Fermi sea in the spin-triplet channel) creates quantum critical charge fluctuations in the excitation spectrum (top boxes, see main text).

Supplementary Materials:

Materials and Methods

Figs. S1 – S6

References (35) – (53)

Supplementary Materials for

Singular charge fluctuations at a magnetic quantum critical point

L. Prochaska[1,*], X. Li[2,#,*], D. C. MacFarland[1,3,§,*], A. M. Andrews[3], M. Bonta[4], E. F. Bianco[5], S. Yazdi[6,$], W. Schrenk[7], H. Detz[7,+], A. Limbeck[4], Q. Si[8], E. Ringe[6,×], G. Strasser[3,7], J. Kono[2,6,8], and S. Paschen[1,8,‡]

[‡]Corresponding author. Email: paschen@ifp.tuwien.ac.at (S.P.)

This PDF file includes:

Materials and Methods
Figs. S1 – S6
References (35) – (53)

Materials and Methods

A. Growth of $YbRh_2Si_2$ thin films on Ge by molecular beam epitaxy

Whereas bulk poly- (*35, 36*) and single crystals (*15, 37–40*) of $YbRh_2Si_2$ have been synthesized by various techniques, the growth of thin films of this material has not been reported. Some bulk crystals, in particular with layered structures, can be lapped into thin samples, but for $YbRh_2Si_2$ thicknesses of about 10 μm reached by polishing down bulk single crystals are much larger than the limit of about 300 nm we estimate for THz transmission experiments on this compound. The bottom up growth of thin films is thus needed for our study.

The technique of choice is molecular beam epitaxy (MBE). We used a Riber Compact 21 MBE system with a growth chamber equipped with two Telemark electron beam evaporation sources for Rh (American Elements, 99.95%) and Si (Dr. Eberl MBE-Komponenten GmbH, resistivity $> 1000\,\Omega$cm), and a low-temperature Knudsen cell for Yb (Ames Laboratory, 99.9%). Inficon quartz thickness monitors as well as a Hiden HAL 114-XBS RC mass spectrometer measure the deposition rates from the two electron beam sources independently. The Knudsen cell beam equivalent pressure is measured by a retractable ion gauge. The growth chamber is pumped to the low 10^{-10} torr range, as monitored by a chamber ion gauge. The total growth rate is limited to avoid (i) spitting behavior of the Rh target at higher powers and (ii) the full melting of the Si target in the carbon crucible because the solubility of carbon in liquid Si (*41*) would introduce impurities if the two were in direct contact.

To set the relative growth rates for achieving the correct 1:2:2 stoichiometry we used feedback from inductively-coupled plasma optical emission spectroscopy (Sect. B) on grown films. Typical growth conditions were beam equivalent pressures of 1.3×10^{-8} torr for Yb, and growth rates of 0.072 Å/s for Si and 0.055 Å/s for Rh as measured by the quartz monitors. Adjusted for the difference in distance to the substrate, this corresponds to a total growth rate of 13 nm/hr.

We selected Ge [fcc, $a = 5.658\,\text{Å}$ (*42*)] as the substrate, because its nearest neighbor distance $a' = a\sqrt{2}/2 = 4.00081\,\text{Å}$ has a lattice mismatch with the lattice parameter of $YbRh_2Si_2$ [$a = 4.011\,\text{Å}$ (*39*)] of only a 0.25% (see Fig. 1A for a sketch of the matching) and because Ge is compatible with the targeted MBE growth conditions. A rough estimate of the critical thickness of the metastable regime, beyond which strained epitaxial layers may relax into a polycrystalline state, is determined by dividing the magnitude of the Burgers vector of the film, $|\vec{\boldsymbol{b}}| = a/\sqrt{2}$, by the lattice mismatch (*43, 44*), yielding 111 nm. Up to this thickness, pseudomorphic growth of $YbRh_2Si_2$ on Ge(100) should thus be possible, which is suitable for our purpose.

3-inch epi-ready Ge substrates were cleaved into quarters and subjected to thermal oxide desorption at 500°C for 2 hours. Prior to each growth, the substrate and material sources were stabilized for a minimum of 2 hours. The growth temperature was 300°C as measured by a thermocouple positioned at the substrate heater.

B. Structural and analytical film characterization

High-resolution X-ray diffraction (HRXRD) with a PANalytical X'Pert system was performed on all films. The system was optimized around the Ge (004) peak and an $\omega - 2\theta$ scan was then recorded. The resulting scans (see Fig. 1B for a typical diffractogram) showed only a single phase in addition to the Ge substrate. The locations of the peaks associated with this phase correspond to the (00l) peaks of $YbRh_2Si_2$ as expected for epitaxial film growth.

A LeBail analysis of the diffraction pattern revealed a lattice parameter $c = 9.8735\,\text{Å}$ which is 0.1% larger than the literature data of $9.858\,\text{Å} \leq c \leq 9.862\,\text{Å}$ (*45*). This analysis was done with PANalytical's HighScore Plus and is similar to a Rietveld refinement, taking into account only the peak positions and disregarding the intensities of the peaks.

The determination of the chemical composition of the films was accomplished by inductively coupled plasma optical emission spectroscopy (ICP-OES). The samples were cleaved

into multiple pieces to allow for the averaging of several runs, and each piece was fully dissolved in a mixture of nitric acid and 10% hydrofluoric acid for enough time to ensure that the film was dissolved. The prepared solutions were then diluted and measured in a Thermo Scientific iCAP 6500 RAD spectrometer. Liquid standards of the individual elements were prepared to calibrate the apparatus. The measured Yb:Rh:Si stoichiometry is 19.9:42.2:37.9 in at%, and 1:2.1:1.9 in atomic ratio. Due to the limited accuracy of this technique (± 5 %) this is consistent with a fully stoichiometric sample.

C. Transmission electron microscopy

Atomic resolution high-angle annular dark field scanning transmission electron microscopy (HAADF-STEM) images were acquired in a double aberration corrected FEI Titan Themis (S)TEM operated at 200 keV. The TEM specimen, with a thickness of less than 50 nm, was prepared using focused ion beam (FIB) milling. The technique of in-situ lift-out was applied in a FEI Helios DualBeam workstation. To minimize effects of the damage caused by the 30 keV Ga ion beam during the thinning process, the surfaces of the thinned sample were subsequently polished with a low-energy (2 keV) Ga ion beam.

The HAADF-STEM image (Fig. 1C) clearly shows high-quality epitaxial growth of the $YbRh_2Si_2$ film on the (45° rotated) Ge substrate. The HAADF signal is approximately proportional to atomic number square (Z^2), and therefore the Yb, Rh, Si, and Ge atomic columns are clearly distinguishable. The interface is remarkably sharp, with minimal (if any) atomic intermixing (Fig. 1D). The overlays shown in Fig. 1C demonstrate how perfectly the complex $YbRh_2Si_2$ lattice is formed. The visualizations of the crystal structures were prepared with VESTA 3 (*46*), which is provided free of charge for academic use.

D. Electrical resistivity

Electrical resistivity measurements were done in a Quantum Design PPMS Model 6000 system with ^{3}He option using the internal resistance bridge to measure the resistivity between 0.5 and 300 K using the van der Pauw technique. The low frequency (17 Hz) of the measurement ensures that these data represent the dc limit. Contacts were made by wire bonding of 25 μm thick gold wires directly onto the film surface. A measurement current of 10 μA was used and confirmed not to lead to self-heating at the lowest measurement temperatures.

E. THz time-domain transmission spectroscopy

In contrast to previous infrared optical conductivity studies that relied on reflection geometry measurements on bulk crystals and subsequent Kramers-Kronig (KK) transformation (*20*), we performed direct phase-resolved THz time-domain transmission spectroscopy measurements on MBE-grown $YbRh_2Si_2$ thin film samples, from which the real and imaginary part of the complex optical conductivity can be directly determined without making assumptions related to the KK relation.

The samples were mounted in a liquid He cryostat with a variable temperature range of $1.4 - 300$ K. THz pulses were generated from a nonlinear (110) zinc telluride crystal pumped by a Ti:sapphire regenerative amplifier (1 kHz, 0.9 mJ, 775 nm, 200 fs, Clark-MXR, Inc., CPA-2001) via optical rectification. A small portion of the laser beam was split to form the probe path. The probe beam was delayed by a mechanical stage, and incident onto a piece of detection zinc telluride crystal together with the transmitted THz beam for probing the THz electric field via the electro-optic sampling method.

In the THz time-domain technique, the THz electric field measured as a function of time can provide both amplitude and phase information. Thus, for a thin film sample whose thickness is much smaller than the THz wavelength and skin depth, both the real (Fig. 3A) and the

imaginary part (Fig. S2) of the optical conductivity can be obtained. The real part is responsible for the THz wave attenuation whereas the imaginary part is typically interpreted as wave phase delay. In the thin film approximation, the complex optical conductivity of the thin film can be expressed as

$$\sigma = \frac{(1 + n_{\text{sub}})[1 - E_{\text{s}}(\omega)/E_{\text{ref}}(\omega)]Y_0}{d \cdot E_{\text{s}}(\omega)/E_{\text{ref}}(\omega)} \tag{S1}$$

where n_{sub} is the refractive index of the substrate, ω is the THz angular frequency, $E_{\text{s}}(\omega)$ and $E_{\text{ref}}(\omega)$ are the Fourier-transformed frequency domain complex electric fields of the THz waves passing through the film on the substrate and through the bare substrate, respectively, Y_0 is the vacuum admittance, and d is thin film thickness.

In this limit, the real part $\text{Re}[\sigma(\omega)]$ is measured to higher accuracy than the imaginary part $\text{Im}[\sigma(\omega)]$, which is why we have focused on $\text{Re}[\sigma(\omega)]$ in the dynamical scaling analysis. Systematic errors on $\text{Im}[\sigma(\omega)]$ are due to the following effects: Firstly, because the film thickness is much smaller than the THz wavelengths, the phase shift of a transmitted THz wave is small. Secondly, the background lattice polarization of the sample is superimposed on the electronic response to give the total $\text{Im}[\sigma(\omega)]$. And finally, even small thickness differences between the sample substrate and the empty substrate used for reference measurements can lead to sizeable errors in $\text{Im}[\sigma(\omega)]$. Either of the latter two effects may be responsible for the negative values of $\text{Im}[\sigma(\omega)]$ we observe at the highest temperatures. By contrast, the $\text{Re}[\sigma(\omega)]$ data agree well with the dc electrical conductivity even at high temperatures, confirming that $\text{Re}[\sigma(\omega)]$ is robust against these effects.

Using $h\nu/(2\pi) \equiv k_B T$ to convert the energy of THz radiation into a thermal energy (*47,48*), our THz frequency range of 0.23 to 2.6 THz corresponds to 1.75 to 20 K. Our criterion for the low-frequency cutoff is that the incident THz signal must be at least two orders of magnitude larger than the noise floor. Our experiments probe $YbRh_2Si_2$ down to an effective minimum

energy scale $E_{\rm min} = \sqrt{(2\pi k_{\rm B} T_{\rm min})^2 + (\hbar\omega_{\rm min})^2}$ that is a factor of 2.3 smaller than that reached in Ref. 20. Together with the high precision of our optical conductivity measurements, this allows for the robust quantum critical scaling analysis we have demonstrated here, which has remained elusive in previous investigations of heavy fermion bulk materials (*49*) and MBE-grown thin films (*50–53*).

F. Residual resistivity correction

For the dc resistivity $\rho(T)$, a subtraction of the residual resistivity can be readily done: The usual approach is to plot the resistivity on a T^α plot that stretches out the curve to a straight line (in the case of $\alpha = 1$, this is simply a linear-linear plot with $\rho = \rho_0 + A'T$). The residual resistivity ρ_0 can be read off such plots as the y-intercept. The basis for this assignment is Matthiessen's rule, which states that the residual scattering rate $1/\tau_{\rm res}$ (due to static disorder or lattice defects) and the intrinsic scattering rate $1/\tau_{\rm in}$ (that in $YbRh_2Si_2$ below about 15 K is dominated by quantum critical fluctuations) are additive.

To generalize the Matthiessen rule to the complex optical conductivity

$$\sigma(\omega, T) = {\rm Re}[\sigma(\omega, T)] + i\,{\rm Im}[\sigma(\omega, T)] \quad , \tag{S2}$$

we suggest the form

$$\sigma_{\rm in}^{-1}(\omega, T) = \sigma^{-1}(\omega, T) - \sigma_{\rm res}^{-1}(\omega) \quad , \tag{S3}$$

where the subscripts in and res denote intrinsic and residual, respectively. $\sigma_{\rm res}^{-1}(\omega)$ is the finite-frequency generalization of the residual resistivity, for which we assume the Drude form

$$\sigma_{\rm res}^{-1}(\omega) = \frac{1 - i\,\omega\tau_{\rm res}}{\sigma_0} \quad \text{with} \quad \sigma_0 = \frac{ne^2\tau_{\rm res}}{m} \tag{S4}$$

that was shown to hold for the heavy fermion compound UPd_2Al_3 (*50*). For our critical scaling analysis of the intrinsic THz and dc data (Fig. 3B, and Fig. S5B on linear scales) with

$$\mathrm{Re}[\sigma_{\mathrm{in}}(\omega,T)]\cdot T^{\alpha}=f(\frac{\hbar\omega}{k_{\mathrm{B}}T}) \tag{S5}$$

we have used $\rho_0 = 11.6\,\mu\Omega$cm (i.e., $\sigma_0 = 8.62\times10^6\,\Omega^{-1}\mathrm{m}^{-1}$; see caption of Fig. 2) and $n = 2.6\times10^{28}\,\mathrm{m}^{-3}$ (*7*) as input parameters, and determined the mass enhancement m/m_0 (where m_0 is the free electron mass) as well as the power α of the scaling relationship. A contour plot of the normalized deviation is shown in Fig. S5A. The data scale best (i.e., show the minimal normalized deviation) at $m/m_0 \approx 130$ and $\alpha \approx 1$. The mass enhancement, that we attribute to the (non-critical) heavy fermion background contribution, is in good agreement with values estimated from an extended Drude analysis of far-infrared data of a bulk $YbRh_2Si_2$ single crystal (*20*). Importantly, the evidenced energy over temperature scaling, with a critical exponent $\alpha \approx 1$, is anchored by a simple fact: The inverse of the real part of the low-temperature intrinsic optical conductivity, $1/\mathrm{Re}(\sigma_{\mathrm{in}})$, is approximately linear in frequency (Fig. S4) just as its dc counterpart is approximately linear in temperature (Fig. 2B).

Finally, we inspect whether dynamical scaling is found also for the imaginary part of the optical conductivity, as expected from it being Kramers-Kronig related to the real part of the optical conductivity. As seen in Fig. S6, this is indeed the case. Best collapse is found for the exponent $\alpha = 1.16$, which is within about 10% of the value obtained when scaling the real part (Fig. 3); in view of the larger uncertainty/systematic errors of the imaginary part (see Sect. E for details) this agreement is satisfying, and demonstrates the internal consistency of our analysis.

Figures

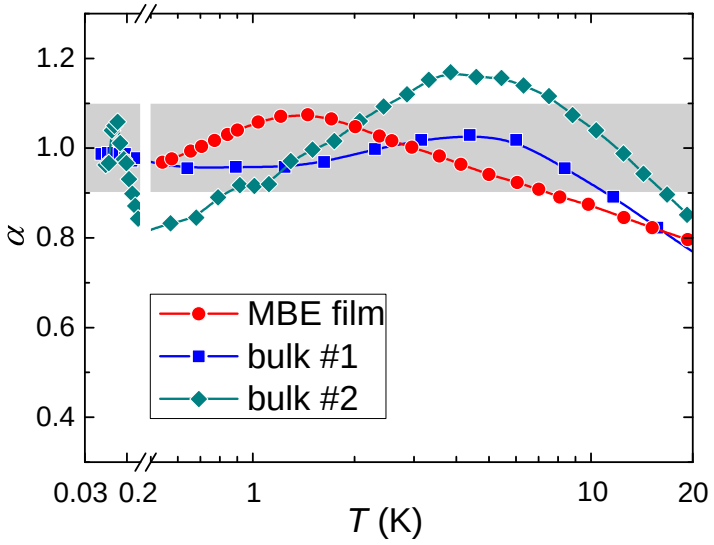

Figure S1: **Exponent from dc electrical resistivity of MBE-grown $YbRh_2Si_2$.** Temperature-dependent exponent α, determined as $\partial \log(\rho - \rho_0)/\partial \log(T)$ for the two samples in Fig. 2, and an additional bulk single crystal (# 2, $\rho_0 = 0.5\,\mu\Omega$cm) (*19*) for comparison. The exponent approaches 1 in the low-temperature limit, but falls below 0.9 above about 8 K for our thin film, and above 11 and 16 K for the two different bulk single crystals (*15, 19*). Within the experimental error bar of $\Delta\alpha \approx 10\%$, all data points below 15 K fall in a zone of $\alpha = 1.0 \pm 0.1$ (grey shading).

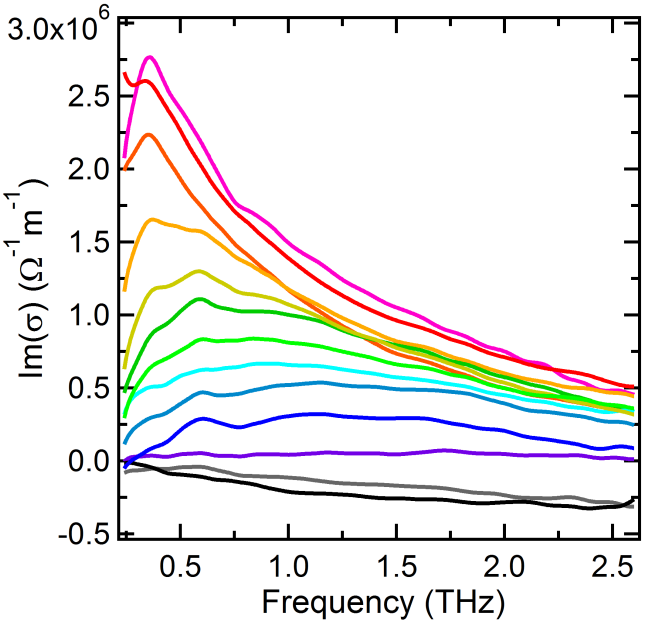

Figure S2: **THz time-domain transmission spectroscopy of MBE-grown $YbRh_2Si_2$.** Imaginary part of optical conductivity, $\mathrm{Im}(\sigma)$, vs frequency at different temperatures (bottom to top: 250, 150, 80, 60, 40, 30, 25, 20, 15, 10, 5, 3, 1.4 K). The strong temperature dependence, setting in below 80 K, echoes the behavior of $\mathrm{Re}(\sigma)$ (Fig. 3A).

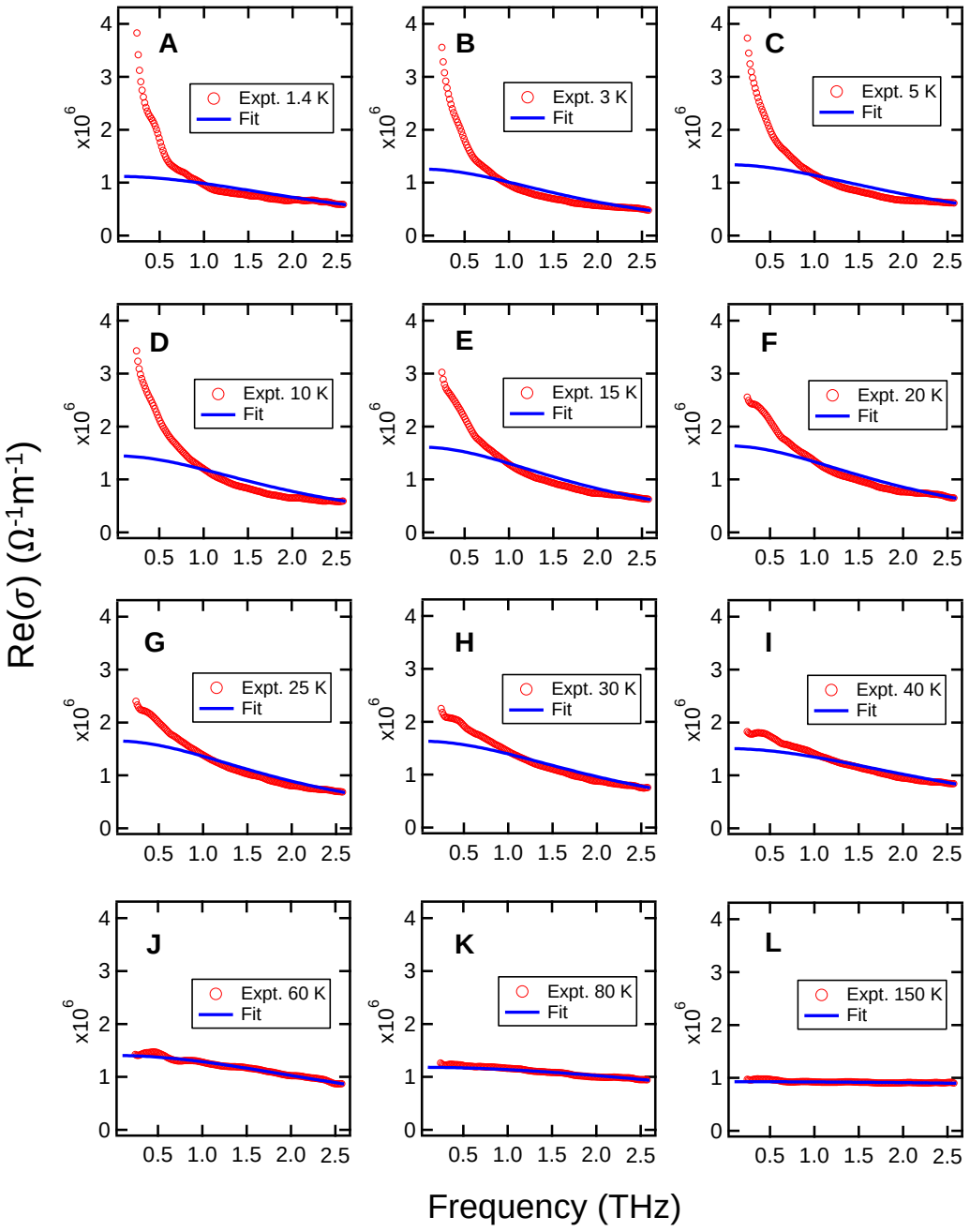

Figure S3: **Non-Drude behavior of optical conductivity at low temperatures.** Re(σ) is well described by the Drude model only at high temperatures. Below 60 K, deviations appear at low frequencies and become increasingly pronounced with decreasing temperature. The fit was pinned to the data at the highest frequency, to illustrate the physically meaningful situation that the deviation develops at low frequencies. A fully free Lorentzian fit does not describe the data anywhere (neither at the low not at the high frequency side; not shown).

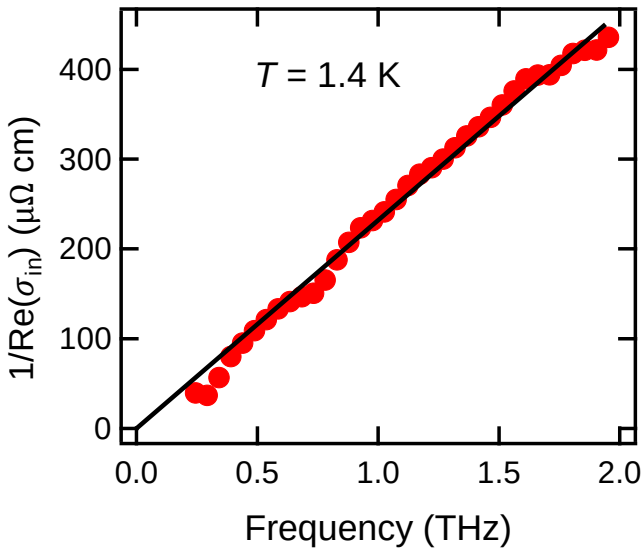

Figure S4: **Linear-in-frequency behavior of inverse real part of the intrinsic optical conductivity of MBE-grown $YbRh_2Si_2$ at the lowest temperature.** $1/\mathrm{Re}(\sigma_{\mathrm{in}})$ is approximately linear in frequency at 1.4 K, as seen by the good agreement between data (points) and a linear fit (line).

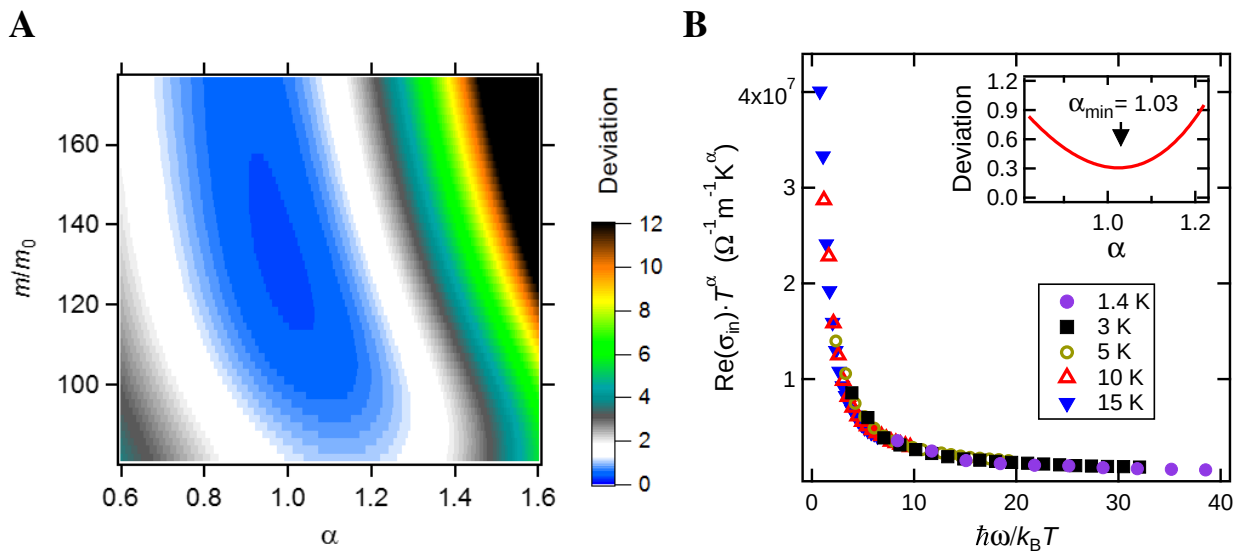

Figure S5: **Scaling analysis of intrinsic optical conductivity of MBE-grown $YbRh_2Si_2$.** (**A**) Contour plot of the normalized deviation as function of the scaling exponent α and the mass enhancement m/m_0 of the Drude contribution due to the residual resistivity, used to determine α (and m/m_0) for optimum scaling. (**B**) ω/T scaling of Fig. 3B replotted on linear scales.

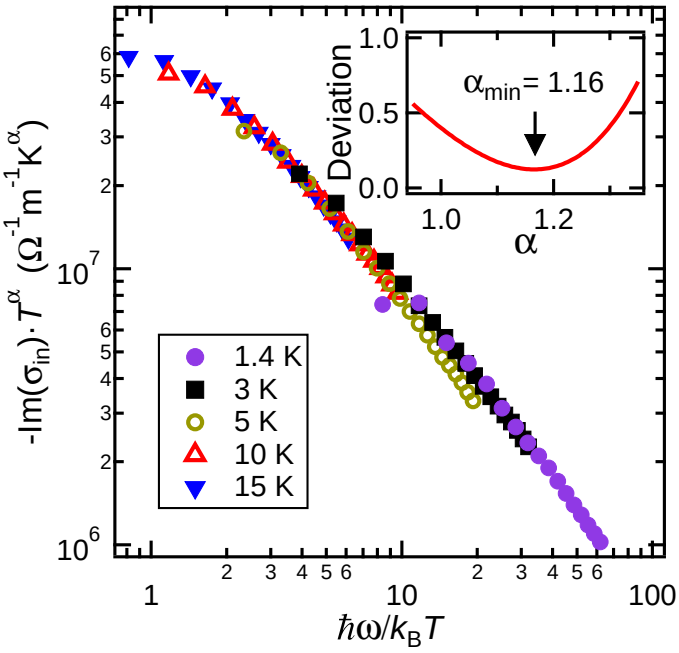

Figure S6: **Scaling analysis of the imaginary part of the optical conductivity of MBE-grown $YbRh_2Si_2$.** The best scaling of $\mathrm{Im}(\sigma_{\mathrm{in}})$ is obtained for $\alpha = 1.16$, within about 10% of the value obtained for the scaling of $\mathrm{Re}(\sigma_{\mathrm{in}})$.